Correlation between ferromagnetic resonance and densification of RE substituted polycrystalline ferrites

Alina Manzoor[a,b,*], Muhammad Azhar Khan[a,**], Wolfgang Kuch[c]

[a] Department of Physics, The Islamia University of Bahawalpur, Bahawalpur 63100, Pakistan
[b] Department of Physics, Government College University, Faisalabad 38000, Pakistan
[c] Institut für Experimentalphysik, Freie Universität Berlin, 14195 Berlin, Germany

A B S T R A C T

We report the dopant- and size-dependent variations in high-frequency magnetic and electrical transport properties of Ho-substituted Li-Mn polycrystalline ferrites. Thermal stability and phase identification were confirmed by thermal gravimetric analysis and X-ray diffraction experiments. The overall average crystallite size decreased from 29.6 to 17.5 nm, whereas the bulk density increased from 3.47 to 4.29 g/cm^3 with increasing Ho content. Ferromagnetic resonance (FMR) measurements at the X-band revealed significant shifts in FMR linewidths and resonance positions as a function of composition. Both, FMR linewidth and porosity, were found to decrease with the systematic addition of Ho from 2538 to 2359 Oe and from 26% to 15.4%, respectively. The substitution of Ho^{3+} for Fe^{3+} reduced the net magnetization of the spinel lattice from 53 to 41 emu/g. Electrical measurements revealed that the resistivity is higher in samples with smaller grains possessing a greater number of thin insulating grain boundaries. The activation energy ΔE required for hopping increases from 0.09 to 0.16 eV with Ho addition, which may be well explained by the increase in resistivity. The substitution of Ho^{3+} for Fe^{3+} causes a decrease in Curie temperature T_c due to the damping of A-B exchange interactions.

1. Introduction

Ferromagnetic resonance (FMR) spectroscopy is used to study the relaxation mechanisms and microwave losses in magnetic nanostructures. Ferrite materials for applications in microwave magnetic devices such as isolator, phase shifter, or circulator are required to possess high resistivity, low microwave losses, and narrow FMR linewidth in order to minimize the heat productivity [1,2]. Microwave relaxation basically yields information on the interactions between the crystal lattice and magnetic excitations. The contributions to such relaxation mechanisms may be isolated into two parts: processes which are related to single crystals and processes which are operative in polycrystalline materials. The basic microwave parameter which serves to characterize the microwave loss in poly-crystals is the FMR linewidth (ΔH). In general, ΔH for polycrystalline ferrite systems is much greater than in the corresponding single crystals of ferrites [3]. In polycrystalline ferrites, the main contribution to ΔH arises from the demagnetizing field induced by porosity and the random orientation of the anisotropy of the grains, given by a sum of three terms [4,5]:

$$\Delta H = \Delta H_k + \Delta H_p + \Delta H_i \tag{1}$$

where ΔH_p and ΔH_k are porosity- and magnetocrystalline-anisotropy-induced line broadenings, respectively. ΔH_i is the intrinsic linewidth, only a few Oersted (< 1 kA/m) in polycrystalline ferrites, and can be ignored. A semiempirical approach was proposed by Sparks [6] to calculate the ΔH_p contribution resulting from the pores.

$$\Delta H_P = 0.17P(3Cos^2\theta_o + 1.4)^2\left(\frac{w}{w_i}\right)\left(\frac{1}{Cos\theta_o}\right)4\pi M_s \tag{2}$$

where P is the ratio of the pores' volume to the sample volume, M_s the saturation magnetization, ω the normalized resonance frequency w.r.t the term $\Upsilon 4\pi M_s$, $\Upsilon = g\mu_B/\hbar$ the gyromagnetic ratio, ω_i the normalized static internal resonance field w.r.t M_s, and θ_o the angle between H_i and the wave vector K of spin waves in the limit of zero wave number (k = 0). E. Schlömann [7] proposed magneto-crystalline anisotropy linebroadening models based on two-magnon scattering theory for two cases; a spin-wave approach ($H_a < 4\pi M_s$) and an independent-grain approach ($H_a > 4\pi M_s$). Weak anisotropy of polycrystalline ferrites suggests the use of the spin-wave approach to evaluate the contribution to ΔH from the magnetocrystalline anisotropy, which can be expressed as follows:

* Corresponding author at: Department of Physics, The Islamia University of Bahawalpur, Bahawalpur 63100, Pakistan.
** Corresponding author.
E-mail addresses: alinamanzoor@hotmail.com (A. Manzoor), azhar.khan@iub.edu.pk (M.A. Khan).

$$\Delta H_k = \frac{2.07}{4\pi M_S} \frac{H_a^2}{}*G(\omega, \omega_i) \tag{3}$$

where $H_a = 2K_1/M_s$ is the anisotropy field, G is a function of frequency (~ 1 at high frequency), and K_1 is the magnetocrystalline anisotropy constant. In view of Eqs. (2) and (3), one can easily separate the microwave loss contribution from the FMR linewidth.

The FMR line-width is greatly affected by the degree of porosity of a magnetic material [1]. Lithium ferrites, partially doped by manganese, are one of the most used compositions in commercial microwave materials [8]. To achieve high densities in lithium-rich ferrites, inclusion of rare-earth (RE) ions into the spinel lattice plays a key role [9–11]. From the point of view of high-frequency applications, the knowledge of ferromagnetic resonance and electrical properties is enormously important. In this context, our work is concentrated on microwave absorption experiments and dc electrical measurements on RE-doped dense polycrystalline ferrite specimens in order to study the disguising influence that the density or porosity may exert in FMR line width and other magnetic and electrical parameters. RE-substituted ferrites yield lower FMR line widths and higher dc resistivity values than the corresponding undoped systems.

2. Experimental

At first, Ho-doped $Li_{1.2}Mn_{.4}Ho_xFe_{2-x}O_4$ ferrites with x = 0.0–0.15 have been synthesized by the sol gel auto combustion method using the following metal precursors: $MnCl_2\cdot H_2O$, $LiCl$, $Ho(NO_3)_3\cdot 5H_2O$, and Fe $(NO_3)_3\cdot 9H_2O$. The desired molar ratios of the raw materials were weighed precisely, while the addition of NH_3 was used to adjust the pH to 7. A citrate-nitrate solution was formed by dissolving the stoichiometric amounts of citric acid and metal nitrates in deionized water. The solution was dried on a hot plate at 80 °C under homogeneous stirring. The subsequent drying of the solution led to the formation of a viscous gel. Then, the viscous gel was self-ignited in an oven at 200 °C, which finally transformed in grey foamy precipitates. After complete ignition, dried precipitates were sintered at 950 °C for 6 h in air for phase formation. Thermal gravimetric and differential thermal analysis (TGA-DTA) was done to estimate the annealing temperature. The identification of crystal structure and phase recognition of the sintered materials was done by X-ray powder diffraction (D8 Advance Bruker, CuKα). The compact circular pellets were pressed from sintered powders in order to study the electrical properties employing a two-probe technique using a Keithley LCR meter model-197. The M-H loops were recorded using a vibrating sample magnetometer Lake-shore model-7300, up to a field of ± 30 kOe, while FMR studies on spherically shaped samples were carried out through an E-LINE century series EPR spectrometer, operating in the X-band (8.9 GHz) at room temperature. The bulk density of circular pellets was determined as:

$$d_b = m/\pi h r^2 \tag{4}$$

where, 'm' is the mass of the pellet, 'h' the pellet thickness and 'r' the radius of the pellet.

3. Results and discussion

3.1. Thermal analysis

The thermal stability of un-sintered powder (x = 0) was assessed by TG-DTA analysis (Mettler Toledo GC 200) from room temperature up to 1000 °C under a heating rate of 10 °C/min. Fig. 1 shows the TGA-DTA curves of the $Li_{1.2}Mn_{0.4}Fe_2O_4$ sample. Two exothermic peaks were observed in the DSC curve at 388 °C and 494 °C, respectively. The exothermic peak around 494 °C is found sharp and intense as compared to the peak at 388 °C, which indicates the melting transition temperature corresponding to complete melting in $Li_{1.2}Mn_{0.4}Fe_2O_4$ ferrite. The energy associated with this melting temperature is basically the enthalpy
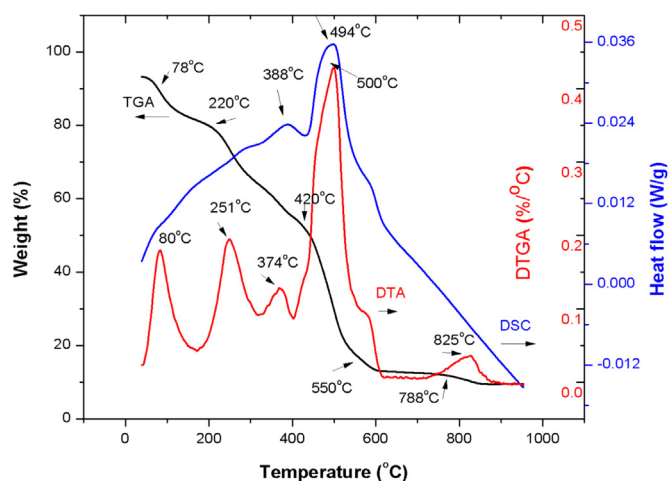

Fig. 1. Thermal analysis of $Li_{1.2}Mn_{0.4}Fe_2O_4$.

of the transition and is connected with the crystallinity of the material [12].

The TGA curve exhibits a total weight loss occurring in the as-prepared sample, which can be ascribed to the decomposition of nitrates and oxides. Above 550 °C, a negligible weight loss confirms the development of a stable phase of the material. The DTA curve shows three main peaks coupled with weight loss: the first at 80 °C is ascribed to the evaporation of absorbed water from the precursor, the peak around 251 °C corresponds to the decomposition of citric acid and inorganic salts, while a prominent exothermic peak at 500 °C corresponds to the decomposition of nitrates and oxides. The majority of the mass loss occurs below 800 °C and an optimized temperature for complete ignition and stable spinel phase formation is found around 950 °C.

3.2. Structural analysis

In Fig. 2 the XRD patterns for all powders calcined at 950 °C show all the expected intense Bragg diffraction lines of the spinel cubic structure belonging to the *Fd3m* space group. No additional peaks other than for the fcc spinel phase were identified for x = 0 composition, confirmed through ICDD card no. 00-049-0266. However, a secondary phase trace $HoFeO_3$ was detected around 2θ = 33° for x ≥ 0.06, matching well with ICDD card no. 01-074-1479. The bigger ionic size of Ho^{3+} than the one of the Fe^{3+} ions prevents the lattice to accommodate higher percentages of Ho^{3+}, and hence, higher Ho doping results in substantial segregation of holmium ions at grain boundaries. This might
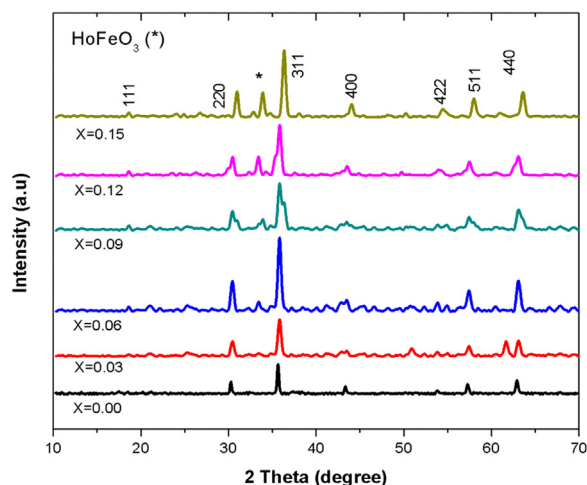

Fig. 2. XRD patterns for $Li_{1.2}Mn_{0.4}Fe_{2-x}H_xO_4$ ferrites.

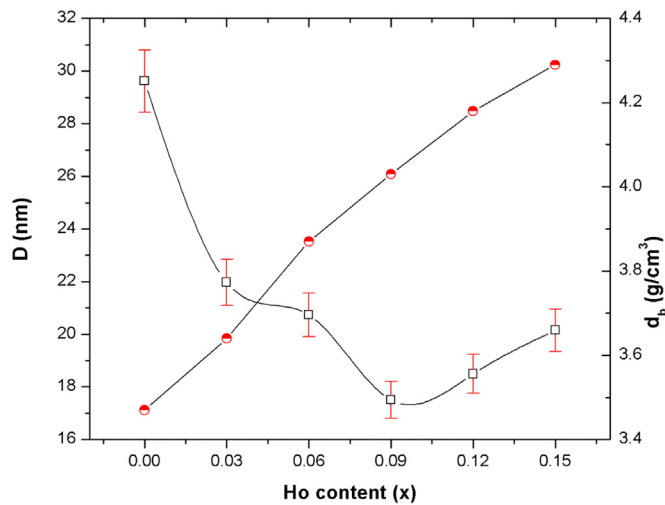**Fig. 3.** Average crystallite size (*D*) and bulk density (*d*$_b$) of the samples with different Ho content.

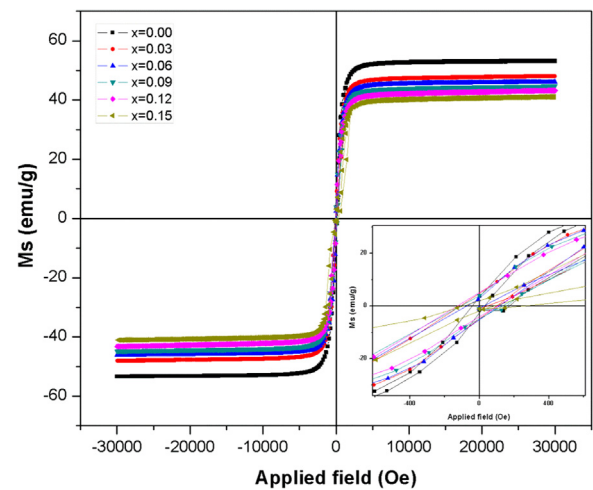**Fig. 4.** M-H hysteresis loops for $Li_{1.2}Mn_{0.4}Fe_{2-x}H_xO_4$ ferrites measured at room temperature. The inset shows a magnified view at low fields.

distort the centro-symmetric fcc structure and contribute to develop the secondary phase at higher concentrations (x ≥ 0.06).

Average crystallite sizes as estimated from the 311 reflection peak using Scherrer's equation are about 29.6–17.5 nm, small enough to obtain a suitable signal-to-noise ratio for various applications [13]. The Nelson-Riley function is used to compute the lattice parameter [14]. The lattice parameter *a* is calculated to change from 8.353- to 8.358 Å up to the substitution of x = 0.03 and then varies from 8.358- to 8.351 Å up to x = 0.15. This increase in lattice parameter is attributed to the expansion of lattice dimensions due to the substitution of larger Ho^{3+} ions for smaller Fe^{3+} ions. The substitution of Ho^{3+} ions into the elastically deformed spinel structure has induced a uniform lattice strain which effectively changes the lattice plane spacing and shifts the diffraction peaks to a lower 2θ position [15]. Moreover, the decrease in *a* led us to conclude that an inter-granular ortho phase compressed the spinel lattice [16]. The increase in bulk density from 3.47 to 4.29 g/cm^3 can be ascribed to the replacement of Fe^{3+} ions with 56 amu weight by Ho^{3+} ions with larger atomic weight (164 amu) on B -sites. Fig. 3 shows the variation of *D* and *d*$_b$ as a function of Ho content. The reduction in porosity (26–15.4%) with increasing Ho concentration indicates the achievement of high densities in the prepared ferrites. The hopping length *L* for magnetic ions (distance between magnetic ions) situated at tetrahedral A -sites and octahedral B -sites is given by [17];

$$L_A = a(\sqrt{3}/4), L_B = a(\sqrt{2}/4) \qquad (5)$$

The hopping length is found to change in a similar fashion as the lattice parameter *a* for increasing Ho^{3+} content. All structural parameters calculated from the XRD measurements are listed in Table 1.

3.3. VSM studies

The static magnetic properties for all samples have been

investigated by VSM at room temperature. Fig. 4 displays curves that exhibit the narrow hysteretic behavior of ferrimagnetic materials. The hysteresis loop properties, such as magnetization, coercive force, and remanence are related to low-frequency magnetization processes. The saturation magnetization M_s decreases systematically, from 53.33 to 41.1 emu/g with increasing Ho content, which indicates the weakening of exchange interactions between magnetic ions with Ho addition. This decrease in M_s can be explained by the cation distribution on A and B sites. The substitution of paramagnetic Ho^{3+} ions replaces the ferromagnetic Fe^{3+} ions on B sites, which results in a dilution of B-sublattice magnetization and subsequently a decrease in overall M_s.

It can be seen from Fig. 5 that the coercivity H_c increases from 36.5 to 118 Oe with Ho concentration up to x = 0.09 and decreases thereafter, displaying an inverse variation with the average grain size [18]. In general, a small grain size results in a higher coercive force due to pinning of domain walls, which requires a higher energy for switching [19]. The values of the remanent magnetization M_r are about 2.1–5.2 emu/g and the anisotropy constant $K_1 = M_s H_c/2$ ranges from 973.3 to 2643.2 erg/cm^3. The strong spin-orbit coupling of Ho^{3+} ions increases the anisotropy constant. For a particular composition, the magnetic moment (n_B) in units of Bohr's magneton is calculated using the relation:

$$n_B = [M_s * M_w]/5585 \qquad (6)$$

where M_s is the saturation magnetization (emu/g), M_w is the molecular weight of a specific composition and 5585 is the magnetic factor. The inclusion of nonmagnetic Ho ions into B -sites decreases the magnetic moment of the B -sublattice in comparison to the magnetic moment of the A -sublattice, which causes a reduction in net magnetic moment of the spinel lattice and hence the magnetization.

Table 1
Structural parameters determined from XRD data for $Li_{1.2}Mn_{0.4}Ho_xFe_{2-x}O_4$ (0.00 ≤ x ≤ 0.15) ferrites.

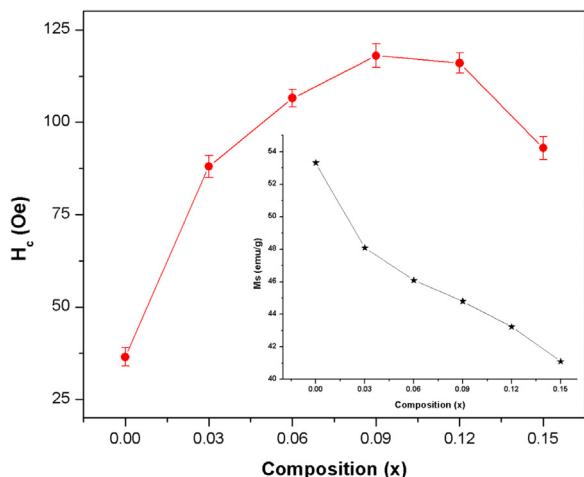| Ho content	Density (g/cm^3)		Lattice parameter	Avg. crystallite size	Porosity	L$_A$	L$_B$
	d_{bulk}	d_{x-ray}	*a* (Å)	*D* (nm)	*P* (%)	(Å)	
x = 0.00	3.47	4.69	8.3534	29.62 ± 1.18	26	3.6170	2.9529
x = 0.03	3.64	4.76	8.3584	21.97 ± 0.88	23.5	3.6191	2.9546
x = 0.06	3.87	4.84	8.3555	20.73 ± 0.83	20.1	3.6179	2.9536
x = 0.09	4.03	4.92	8.3541	17.5 ± 0.71	18	3.6137	2.9531
x = 0.12	4.18	4.99	8.3523	18.49 ± 0.74	16.3	3.6165	2.9525
x = 0.15	4.29	5.07	8.3514	20.15 ± 0.81	15.4	3.6161	2.9522

Fig. 5. Change in coercivity (H_c) as a function of composition (x). The inset shows the variation in saturation magnetization M_s with the composition.

3.4. Ferromagnetic resonance studies

The FMR technique at the X-band (8.9 GHz) was employed to characterize the microwave losses in the ferromagnetic materials. Microwave resonance properties, such as the FMR linewidth (ΔH) and FMR position (H_{res}) are related to high-frequency relaxation processes. Such microwave properties rely on microstructural considerations such as material processing factors, porosity and grain size, and electrical properties as well as intrinsic parameters [20]. The peak-to-peak FMR linewidth ΔH_{pp} (Fig. 6) is caused mainly by two mechanisms: magnetic inhomogeneities of the ferromagnet and the intrinsic damping of magnetization [21]. The resonance signal (inset of Fig. 6) as measured from the absorption curve resembles a Lorentzian lineshape. Fig. 7 shows the room-temperature FMR spectra of different compositions as a function of Ho content, usually measured by the absorption derivative ($d\chi/dH$). It is noted that with increase in iron deficiency (increasing Ho content), ΔH (ΔH_{pp}) reduces from 2538- to 2360 Oe. This decrease in ΔH is consistent with the reduction in porosity and the increase in density as shown in Fig. 8. This change in ΔH as a function of Ho concentration also coincides with the behavior of M_s.

Due to the weak magnetocrystalline anisotropy of polycrystalline ferrites, the line broadening due to pores ΔH_p constitutes an important contribution to ΔH and dominates over the linebroadening arising from crystalline anisotropy ΔH_k. Thus, in polycrystalline ferrites with weak
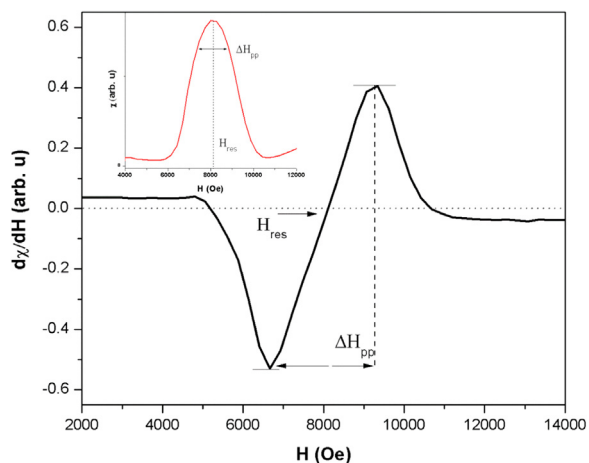

Fig. 6. FMR absorption curve derivative ($d\chi/dH$) Vs applied field (H) for $Li_{1.2}Mn_{0.4}Fe_2O_4$. The inset shows the integral of the FMR absorption curve for $Li_{1.2}Mn_{0.4}Fe_2O_4$.
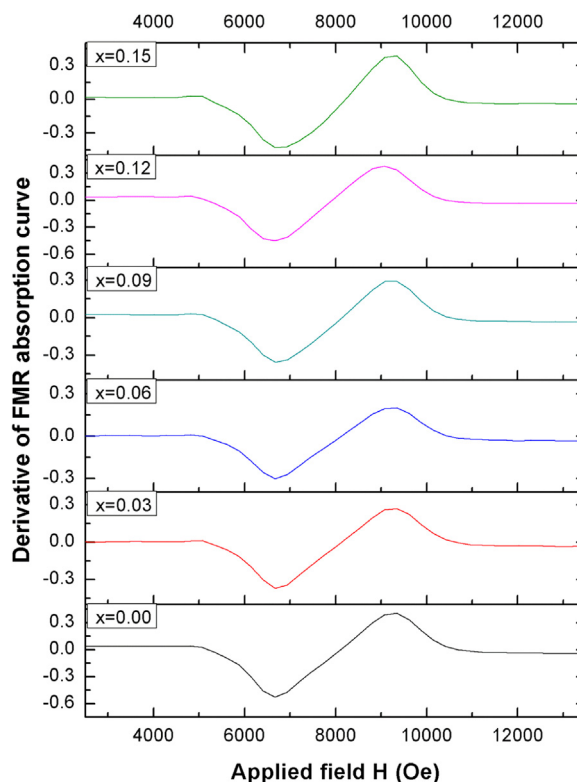

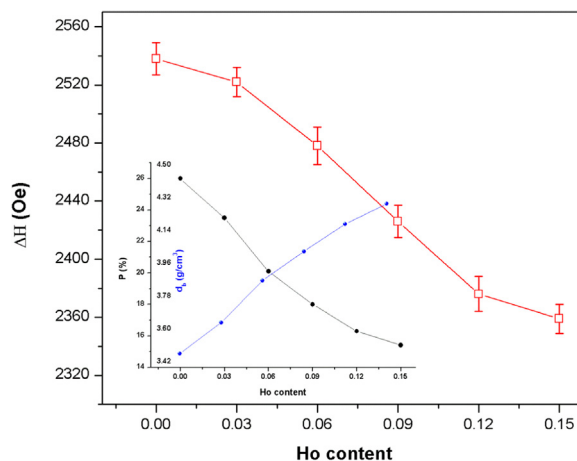**Fig. 7.** Room-temperature FMR absorption spectra for $Li_{1.2}Mn_{0.4}Fe_{2-x}H_xO_4$ ferrites.

Fig. 8. Variation of FMR line width ΔH with Ho content. The inset shows the variations in % of porosity and bulk density with Ho concentration.

anisotropy, a dense and uniform microstructure is the significant approach to cut down ΔH. However, these values of ΔH are greater than those reported for single crystals of Li-rich ferrites [22], which had been attributed to a random distribution of the anisotropy axis in the polycrystalline state. The values of the resonance field H_{res} show a random variation. In polycrystalline materials, the existence of pores and the random orientation of crystallites cause H_{res} to vary from point to point within the material, which shifts and broadens the resonance line [23]. The intensities of the FMR profiles depend on the morphology and the gyromagnetic ratio (γ), which further depends on the spectroscopic splitting factor g for various cations, i.e. $\gamma = g\mu_B/\hbar$ [24]. Table 2 summarizes the static and dynamic magnetic parameters obtained from the VSM and FMR measurements, respectively.

Table 2

Magnetic parameters for all investigated compositions of $Li_{1.2}Mn_{0.4}Ho_xFe_{2-x}O_4$ ferrites with x = 0.00–0.15.

| Ho concentration	Dynamic magnetic parameters (FMR)		Static magnetic parameters (VSM)				
	ΔH (Oe)	H_{res} (Oe)	M_s (emu/g)	H_c (Oe)	$R = M_r/M_s$	K_1 (erg/cm^3)	n_B (μ_B)
x = 0.00	2538 ± 11	8091	53.33	36.5 ± 2.5	0.06375	973.27	1.96
x = 0.03	2522 ± 10	8087	48.1	88 ± 3	0.09771	2116.40	1.80
x = 0.06	2478 ± 13	8175	46.1	106.5 ± 2.4	0.06074	2454.83	1.75
x = 0.09	2426 ± 11	8144	44.8	118 ± 3.2	0.08482	2643.20	1.73
x = 0.12	2376 ± 12	7912	43.24	116 ± 2.7	0.12026	2507.92	1.69
x = 0.15	2359 ± 10	8236	41.1	93 ± 3.1	0.05109	1911.15	1.63
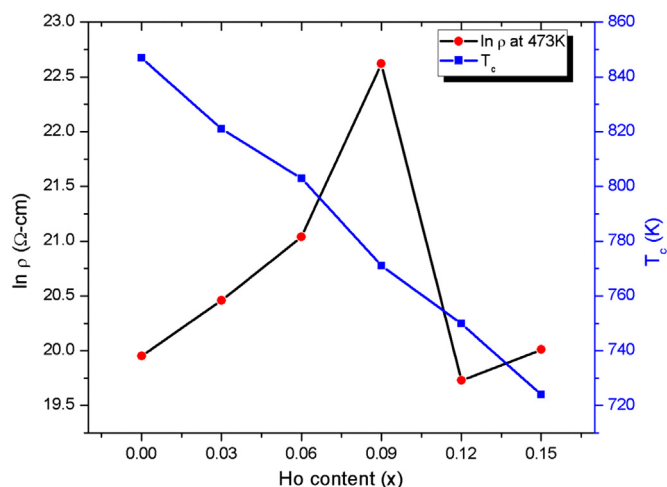
Fig. 9. Dc electrical resistivity and Curie temperature T_c for all compositions.

3.5. Electrical properties

3.5.1. Composition-dependent dc resistivity

The dc electrical resistivity of Ho-substituted ferrites is measured by the following relation:

$$\rho = RA/l \tag{7}$$

where R is the resistance, A the area of the pellet, and l the pellet thickness

Fig. 9 shows the room-temperature behavior of ρ_{dc} vs Ho content (x). ρ increases from 4.6×10^8 to 6.7×10^9 Ω cm up to x = 0.09 and decreases thereafter. This observed electrical behavior may be due to the cation occupancy of Fe^{3+}, Mn^{2+}, and Ho^{3+} as well as their migration among the A and B -sites due to Ho substitution. The hopping probability of charged species depends upon the activation energy of hopping and the number of Fe^{2+}/Fe^{3+} ion pairs present on B -sites. Upon Ho incorporation for Fe into the spinel lattice, a part of Ho^{3+} ions tends to occupy the B -sites. The substitution of Ho in place of iron decreases the concentration of Fe^{3+} ions at B -sites, thereby decreasing the hopping rate of electron transfer between Fe^{2+} and Fe^{3+} ions and subsequently reducing the conduction process [25]. Hence ρ_{dc} increases with the increase of Ho content. In addition, Ho has a high value of ρ (9.4×10^{-7} m Ω) as compared to iron Fe (9.7×10^{-8} m Ω), which may contribute to raise the resistivity of the Ho-substituted ferrites. When larger Ho^{3+} ions try to replace the smaller Fe^{3+} ions, the deviation from structural stoichiometry causes a lattice distortion. This lattice distortion produces a change in electrical properties of materials keeping the composition and structure constant according to the parent crystal structure [26,27]. The dc electrical resistivity of ferrite systems depends on various micro-structural parameters like porosity, stoichiometry, grain size, and grain boundaries. For smaller grains with a greater surface-to-volume ratio, oxidation occurs faster and re-conversion of Fe^{2+} ions (created during sintering) back to Fe^{3+} may take place. Hence, the survival of Fe^{2+} ions is less likely in smaller-grained samples [28,29]. Moreover, small grains in particular involve a large number of insulating thin grain boundaries, which act as scattering centers to the flow of electric charge carriers, hence, reducing the electron exchange between $Fe^{2+} \leftrightarrow Fe^{3+}$ and thus, raising the resistivity [30,31]. The decrease in resistivity can be attributed to the solubility limit of Ho^{3+} ions in the spinel lattice as well as the segregation of some Ho^{3+} ions at the grain boundaries resulting in a lower number of Ho^{3+} ions available to substitute for Fe^{3+} ions on B -sites.

3.5.2. Temperature-dependent dc resistivity

The temperature-dependent ρ_{dc} for the temperature range 473–973 K is shown in Fig. 10. The temperature-dependent electrical resistivity in ferrites is associated with hopping of electrons and charge transport via excited states which can be stated using the Arrhenius equation as:

$$\rho = \rho_o exp(\Delta E/k_B T) \tag{8}$$

where ρ_o is the resistivity extrapolated to infinite temperature, T the absolute temperature, k_B the Boltzmann constant, and ΔE represents the activation energy calculated from a linear fitting of the Arrhenius plot. It can be seen from $log\,\rho$ vs. $1000/T$ plots that the resistivity starts to decrease linearly by increasing the temperature which ensures the typical semiconducting nature of the prepared ferrites [32]. This decrease in resistivity can be attributed to the increase of thermally activated drift mobility of conduction charge species which are thermally activated with the increase in temperature [33,34].

3.5.3. Activation energies

The energy barrier that a conduction electron is required to overcome for successful hopping is termed the activation energy. The activation energy ΔE is calculated from the slope of the Arrhenius plots for
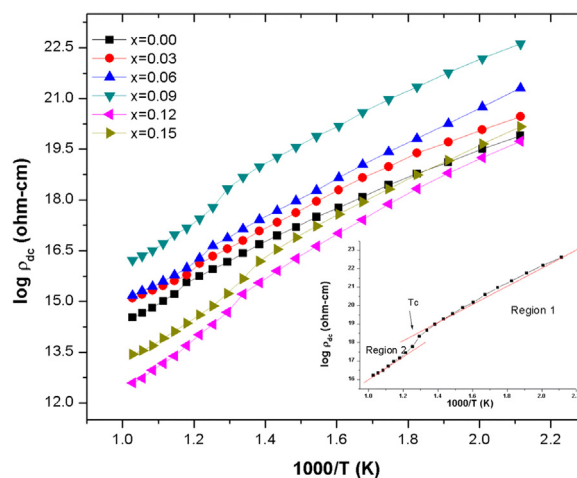

Fig. 10. Temperature-dependent resistivity behavior for all samples. In inset part (x = 0.09), a change in slope at T_c designates a ferromagnetic to paramagnetic transition.

Table 3
Temperature-dependent electrical parameters of $Li_{1.2}Mn_{0.4}Ho_xFe_{2-x}O_4$ ferrites with x = 0.00–0.15.

Ho content	ρ_{dc} (Ω-cm) at 473 K	T_c (K)	E_p (eV)	E_f (eV)	Activation energy (eV) $\Delta E = E_p - E_f$	μ_d (cm²/V s) at 473 K
x = 0.00	4.62×10^8	847	1.03336	0.93369	0.09966 ± 0.0029	6.66×10^{-13}
x = 0.03	7.67×10^8	821	1.0907	0.97384	0.11686 ± 0.0035	3.95×10^{-13}
x = 0.06	1.37×10^9	803	1.16948	1.03295	0.13654 ± 0.0041	2.14×10^{-13}
x = 0.09	6.68×10^9	771	1.25469	1.08866	0.16603 ± 0.0049	4.36×10^{-14}
x = 0.12	3.71×10^8	750	1.19358	1.06409	0.12949 ± 0.0038	7.79×10^{-13}
x = 0.15	4.92×10^8	724	1.20726	1.07401	0.13325 ± 0.004	5.91×10^{-13}

various compositions using the relation:

$$\Delta E = slopex \quad 2.303 \quad xk_Bx10^3 \tag{9}$$

where $k_B = 8.62 \times 10^{-5}$ eV/K is the Boltzmann constant. As can be seen from the Arrhenius plots (Fig. 10), the slope of the resistivity curve changes at higher temperatures by a kink that divides the curve into two regions; ferrimagnetic (region 1) and paramagnetic (region 2). The variation of ρ is linear up to a certain temperature where an anomaly occurs, depicting the transition temperature, known as Curie temperature T_c. The Curie point designates a transition of magnetic ordering from ferrimagnetic to paramagnetic behavior in ferrites. The region 1 below T_c is called ferrimagnetic region while region 2 above T_c corresponds to the paramagnetic region. The activation energies calculated for both regions separately are summarized in Table 3. It can be seen from Fig. 11 that the activation energies are in the range of 0.09–0.16 eV. The composition with high resistivity has also a large value of activation energy and vice versa [35].

Activation energies associated with the paramagnetic region (E_p) are higher than those of the ferrimagnetic region (E_f) and are consistent with the theory of Irkhin and Turov of magnetic semiconductors [23]. According to Irkhin and Turov, the paramagnetic state, being a disordered state, should have larger activation energy than the ferrimagnetic state, which is more ordered [2]. As a consequence, conduction species require more energy for conduction in the paramagnetic region than in the ferrimagnetic region. Thus, it is clear that the process of conduction is affected by a change in magnetic ordering. Similar results have been reported earlier, obtained for a number of mixed ferrites [24–26]. The calculated values of activation energies of all investigated samples are comparable to those of the trivalent rare-earth-substituted ferrites [27].

3.5.4. Curie temperature T_c

T_c for all ferrite samples is determined and tabulated in Table 3. It has been observed that T_c tends to decrease with increase in Ho content. This change in T_c depend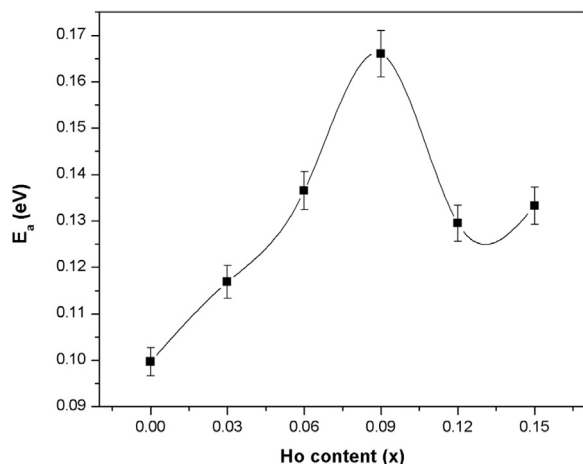s on the number of magnetic ions present on tetrahedral sites, octahedral sites, and the exchange interactions between them. The incorporation of Ho^{3+} ions replaces the Fe^{3+} ions residing on the octahedral sites. The increasing concentration of Ho^{3+} ions at the octahedral site reduces the number of Fe^{3+} ions, which results in the weakening of A-B super exchange interactions. Since the overall strength of the A-B exchange interaction determines the Curie temperature, the damping of A-B interactions upon Ho addition results in a decrease of T_c.

3.5.5. Drift mobility μ_d

The charge carrier concentration (n) and drift mobility (μ_d) for all compositions are calculated using the following relations [28,29]:

$$n = N_a\rho_b P_{Fe}/M \tag{10}$$

$$\mu_d = 1/ne\rho \tag{11}$$

where N_a is the Avogadro number, ρ_b is the bulk density of sintered pellets, M is the molecular weight of the sample, P_{Fe} represents the number of iron atoms in the chemical formula and e is the charge of an electron. μ_d is found to decrease from 6.6×10^{-13} to 4.3×10^{-14} cm² $V^{-1} S^{-1}$ with increase in Ho concentration up to x = 0.09. Variation in μ_d as a function of temperature is given in Fig. 12. It has been observed that the compositions with higher resistivity have lower values of μ_d and vice versa. Furthermore, μ_d indicates a direct relation with temperature as the mobility of charge species increases with increasing temperature. However, n changes only slightly with composition and temperature, which implies that, it is the change in μ_d of charge carriers that is accountable for the variation of ρ rather than the change in n. Therefore, as the temperature increases, hopping of charge carriers from one site to another starts, resulting in an increase in the carrier's mobility and a decline in resistivity.

4. Conclusions

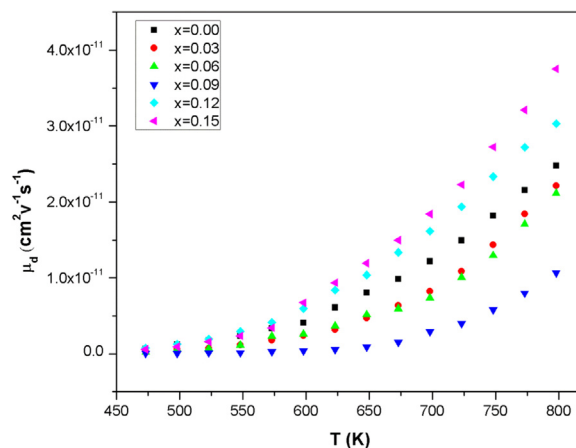In the limit of week crystalline anisotropy of polycrystalline ferrites,

Fig. 11. Activation energy (E_a) for all samples as a function of Ho content.

Fig. 12. Temperature dependence of drift mobility for $Li_{1.2}Mn_{0.4}Fe_{2-x}H_xO_4$ ferrites.

a dense and uniform microstructure is an optimum approach to diminish the FMR linewidth ΔH. The line broadening of Ho-substituted lithium-rich ferrites has been found to decrease with the decrease in porosity and the increase in material density. A significant change in H_{res} and M_s has been observed with systematic inclusion of Ho ions. Electrical analysis has proven that the microstructure with small grains reveals low resistivity values and vice versa. The variation of dc resistivity with temperature confirms the low mobility and the semiconducting nature of the prepared ferrites. The damping of A-B interactions upon Ho addition results in a decrease of T_c. Such RE-substituted high-density ferrites, in contrast to un-substituted ferrites, reveal narrow FMR linewidth, high resistivity, and low microwave losses, which is prerequisite for their use in microwave applications.

Acknowledgment

References

[1] K. Sun, Z. Pu, Y. Yang, L. Chen, Z. Yu, C. Wu, X. Jiang, Z. Lan, Rietveld refinement, microstructure and ferromagnetic resonance linewidth of iron-deficiency NiCuZn ferrites, J. Alloy. Compd. 681 (2016) 139–145.

[2] L. Jia, Y. Zhao, F. Xie, Q. Li, Y. Li, C. Liu, H. Zhang, Composition, microstructures and ferrimagnetic properties of Bi-modified LiZnTiMn ferrites for LTCC application, AIP Adv. 6 (2016) 056214.

[3] V.G. Harris, Modern microwave ferrites, IEEE Trans. Magn. 48 (2012) 1075–1104.

[4] P. Roschmann, Separation of anisotropy and porosity contributions to inhomogeneous broadened FMR linewidth in polycrystalline YIG, IEEE Trans. Magn. 11 (1975) 1247–1249.

[5] R. Guo, Z. Yu, Y. Yang, X. Jiang, K. Sun, C. Wu, Z. Xu, Z. Lan, Effects of Bi_2O_3 on FMR linewidth and microwave dielectric properties of LiZnMn ferrite, J. Alloy. Compd. 589 (2014) 1–4.

[6] M. Sparks, Ferromagnetic resonance porosity linewidth theory in polycrystalline insulators, J. Appl. Phys. 36 (1965) 1570–1573.

[7] E. Schlömann, Spin-wave analysis of ferromagnetic resonance in polycrystalline ferrites, J. Phys. Chem. Solids 6 (1958) 242–256.

[8] P. Kumar Dipti, J.K. Juneja, S. Singh, K.K. Raina, C. Prakash, Improved dielectric and magnetic properties in modified lithium-ferrites, Ceram. Int. 41 (2015) 3293–3297.

[9] Z.A. Gilani, M.S. Shifa, M.A. Khan, M.N. Anjum, M.N. Usmani, R. Ali, M.F. Warsi, New LiCo0. 5PrxFe2- xO4 nanoferrites: prepared via low cost technique for high density storage application, Ceram. Int. 44 (2018) 1881–1885.

[10] M.K. Abbas, M.A. Khan, F. Mushtaq, M.F. Warsi, M. Sher, I. Shakir, M.F.A. Aboud, Impact of Dy on structural, dielectric and magnetic properties of Li-Tb-nanoferrites synthesized by micro-emulsion method, Ceram. Int. 43 (2017) 5524–5533.

[11] S. Lature, S. Kalashetty, G. Jadhav, Structural, thermoelectric power and magnetization measurements of Nd-doped Li–Ti ferrite by combustion synthesis, Phys. Scr. 90 (2015) 085805.

[12] C.V. Reddy, C. Byon, B. Narendra, D. Baskar, G. Srinivas, J. Shim, S.P. Vattikuti, Investigation of structural, thermal and magnetic properties of cadmium substituted cobalt ferrite nanoparticles, Superlattices Microstruct. 82 (2015) 165–173.

[13] R. Rosnan, Z. Othaman, R. Hussin, A.A. Ati, A. Samavati, S. Dabagh, S. Zare, Effects of Mg substitution on the structural and magnetic properties of Co0. 5Ni0. 5- x Mg x Fe2O4 nanoparticle ferrites, Chin. Phys. B 25 (2016) 047501.

[14] I. Ali, M. Islam, M. Ishaque, H.M. Khan, M.N. Ashiq, M. Rana, Structural and magnetic properties of holmium substituted cobalt ferrites synthesized by chemical co-precipitation method, J. Magn. Magn. Mater. 324 (2012) 3773–3777.

[15] V. Rathod, A. Anupama, V. Jali, V. Hiremath, B. Sahoo, Combustion synthesis, structure and magnetic properties of Li-Zn ferrite ceramic powders, Ceram. Int. 43 (2017) 14431–14440.

[16] A. Zubair, Z. Ahmad, A. Mahmood, W.-C. Cheong, I. Ali, M.A. Khan, A.H. Chughtai, M.N. Ashiq, Structural, morphological and magnetic properties of Eu-doped CoFe2O4 nano-ferrites, Results Phys. 7 (2017) 3203–3208.

[17] M. Satalkar, N. Ghodke, S. Kane, Influence of high temperature sintering on the structural and magnetic Properties of Mn1 − xZnxFe2O4, J. Phys.: Conf. Ser. (2014) 012016 (IOP Publishing).

[18] A. Manzoor, M.A. Khan, M. Shahid, M.F. Warsi, Investigation of structural, dielectric and magnetic properties of Ho substituted nanostructured lithium ferrites synthesized via auto-citric combustion route, J. Alloy. Compd. 710 (2017) 547–556.

[19] M.S. Shah, K. Ali, I. Ali, A. Mahmood, S.M. Ramay, M.T. Farid, Structural and magnetic properties of praseodymium substituted barium-based spinel ferrites, Mater. Res. Bull. 98 (2018) 77–82.

[20] M.A. Khan, Mu Islam, M.A. Iqbal, M. Ahmad, M.F. Din, G. Murtaza, I. Ahmad, M.F. Warsi, Magnetic, ferromagnetic resonance and electrical transport study of Ni1 −xTbxFe2O4 spinel ferrites, Ceram. Int. 40 (2014) 3571–3577.

[21] M. Farle, Ferromagnetic resonance of ultrathin metallic layers, Rep. Progress. Phys. 61 (1998) 755.

[22] N. Pachauri, B. Khodadadi, M. Althammer, A.V. Singh, B. Loukya, R. Datta, M. Iliev, L. Bezmaternykh, I. Gudim, T. Mewes, Study of structural and ferromagnetic resonance properties of spinel lithium ferrite (LiFe5O8) single crystals, J. Appl. Phys. 117 (2015) 233907.

[23] M.A. Khan, Mu Islam, M.A. Iqbal, M. Ahmad, M.F. Din, G. Murtaza, I. Ahmad, M.F. Warsi, Magnetic, ferromagnetic resonance and electrical transport study of Ni 1 − x Tb x Fe 2 O 4 spinel ferrites, Ceram. Int. 40 (2014) 3571–3577.

[24] M.A. Khan, M. ul Islam, M.A. Iqbal, M. Ahmad, M.F. Din, G. Murtaza, I. Ahmad, M.F. Warsi, Magnetic, ferromagnetic resonance and electrical transport study of Ni1 − xTbxFe2O4 spinel ferrites, Ceram. Int. 40 (2014) 3571–3577.

[25] E. Rezlescu, N. Rezlescu, P. Popa, L. Rezlescu, C. Pasnicu, The influence of R2O3 (R = Yb, Er, Dy, Tb, Gd, Sm and Ce) on the electric and mechanical properties of a nickel–zinc ferrite, Phys. Status Solidi A 162 (1997) 673–678.

[26] M. Maisnam, S. Phanjoubam, C. Prakash, Electrical properties of Cd 2 + substituted Li–Zn ferrites, Mod. Phys. Lett. B 24 (2010) 2195–2200.

[27] E. Pervaiz, I. Gul, High frequency AC response, DC resistivity and magnetic studies of holmium substituted Ni-ferrite: a novel electromagnetic material, J. Magn. Magn. Mater. 349 (2014) 27–34.

[28] N. Chandamma, B. Manohara, B. Ujjinappa, G. Shankarmurthy, M.S. Kumar, Structural and electrical properties of Zinc doped Nickel ferrites nanoparticles prepared via facile combustion technique, J. Alloy. Compd. 702 (2017) 479–488.

[29] S. Abbas, A. Munir, F. Zahra, M. Rehman, Enhanced electrical properties in Nd doped cobalt ferrite nano-particles, IOP Conf. Ser.: Mater. Sci. Eng. (2016) 012027 (IOP Publishing).

[30] A.K. Singh, A. Verma, O. Thakur, C. Prakash, T. Goel, R. Mendiratta, DC resistivity of Mn–Ni–Zn ferrites, Jpn. J. Appl. Phys. 41 (2002) 5142.

[31] A. Bhaskar, B.R. Kanth, S.R. Murthy, Preparation of low–power loss MgCuZn ferrites using the microwave sintering method, J. Mater. Sci. 39 (2004) 3787–3791.

[32] J.S. Kounsalye, A.V. Humbe, P.P. Khirade, A.R. Chavan, K. Jadhav, Rietveld refinement and electrical properties of LiTiFeO4, AIP Conference Proceedings, AIP Publishing, 2017, pp. 050123.

[33] M. Maisnam, S. Phanjoubam, Higher dc resistivity of Li-Zn-Cd ferrites prepared by microwave sintering compared with conventional sintering, Bull. Mater. Sci. 37 (2014) 1227–1232.

[34] M.T. Rahman, C. Ramana, Impedance spectroscopic characterization of gadolinium substituted cobalt ferrite ceramics, J. Appl. Phys. 116 (2014) 164108.

[35] M. El-Shabasy, DC electrical properties of Zn-Ni ferrites, J. Magn. Magn. Mater. 172 (1997) 188–192.